Identification of a percolationlike critical region in the decay of excited calcium nuclei

P. Désesquelles, A. J. Cole, A. Giorni, D. Heuer, A. Lleres, and J. B. Viano
Institut des Sciences Nucléaires, IN2P3-CNRS et Université Joseph Fourier, 53 Avenue des Martyrs, F-38026 Grenoble Cedex, France

B. Chambon, B. Cheynis, D. Drain, and C. Pastor
Institut de Physique Nucléaire, IN2P3-CNRS et Université Claude Bernard, 43 Boulevard du 11 Novembre 1918, F-69622 Villeurbanne Cedex, France
(Received 25 January 1993)

The multidetector AMPHORA was used to investigate the reaction of 35 MeV per nucleon ^{40}Ca ions with a ^{nat}Cu target. For 150 000 events corresponding to peripheral and midperipheral collisions, it was possible to reconstruct the primary projectilelike fragments and to calculate event by event the center of mass and the excitation energy. Comparison with a percolation simulation (charge moments, critical exponent) and a momentum ellipsoid analysis are presented and commented. No evidence for a change in disintegration mechanism with increasing excitation energy is found.

PACS number(s): 25.70.Pq, 25.70.Mn

I. INTRODUCTION

The study of highly excited atomic nuclei [1–3] is presently one of the most active fields in heavy-ion-collision physics. The global objective of such studies is to understand how the evolution (decay) of such nuclei is influenced by temperature, compression and rotation (which are the main forms of excitation energy produced by collisions). From the experimental point of view, excited nuclei are produced either by incomplete fusion in central collisions or in very inelastic (quasi)binary reactions. In the former case, in which hot nuclei are formed with low angular momenta, a considerable fraction of the excitation energy may be initially stored as compressional energy [4,5] whereas the latter situation usually involves significant rotational energy imparted to the projectilelike and targetlike fragments. In heavy nuclei, the possibility of observing a thermally induced Coulomb instability has also been invoked [6].

For quasibinary collisions, which are the subject of the present work, it is quite challenging to understand how kinetic energy and orbital angular momentum in the entrance channel are converted into internal excitation and rotation of the primary fragments. However, in this study, we will concentrate on the disintegration mechanism of the primary projectilelike fragments (PPLF's). At low excitation energies, experimental measurements of evaporation residues and light particles produced in fusion reactions are well described by the multistep Hauser-Feshbach formalism [7] which, however, becomes inadequate for excitation energies greater than $\sim$3 MeV per nucleon where the emission of intermediate mass fragments (which themselves may further decay) may compete significantly with light particle ($Z < 3$) emission [8]. At excitation energies greater than 5 MeV per nucleon, the time scale for particle emission may become comparable with the time necessary for a given emitted fragment to escape from the vicinity of the parent and may even be comparable with typical equilibration times [9,10], so that the usual sequential or binary sequential equilibrium statistical decay models [11] may no longer be useful. Statistical multifragmentation models [12] may then be invoked providing that the initially excited parent nuclei can be considered to be in equilibrium.

Study of the disintegration mechanism of primary projectilelike collision products is greatly facilitated by the use of multidetector systems [13–15] insofar as certain quantities such as the identity, the excitation energy, and the location of the center of mass of primary projectilelike fragments moving with velocities somewhat inferior to the beam particles can be explicitly reconstructed from the decay products. Thus, the need for a detailed model for the formation of hot PPLF's is obviated, although of course it remains possible to compare the predictions of such models with the experimental observations. Unfortunately the angular momentum transferred to the PPLF cannot be directly measured and, in most cases, this fact leads to the introduction of corresponding parameters in the decay calculations.

The measurements to be presented and discussed herein constitute part of a data set obtained with the multidetector AMPHORA [16] in the reaction ^{40}Ca + ^{nat}Cu at 35 MeV per nucleon. The experiment is presented in the following section. The data reduction procedures and, in particular, the separation of the projectilelike fragments (PLF's) with total detected charge 20, and excitation energies up to 7.5 MeV per nucleon (150 000 events), are presented in Sec. III. Intermediate mass fragment production is described in Sec. IV. In Sec. V, we compare various aspects of the measured charge distributions with those obtained from a simple bond breaking (percolation) calculation. This analysis is obviously only one of many that could be performed with the data. Indeed we are in the process of comparing our data with statistical model predictions [17]. However, in the present work, we report only on the percolation analysis.

It is shown that the sample of physical events under study reaches an excitation energy equivalent to the percolation critical bond-breaking probability. In Sec. VI, we search for evidence for a mechanism transition close to this so-called critical energy using dynamical variables. The momentum ellipsoid analysis of the PPLF decay products does not seem consistent with multifragmentation. In Sec. VII we summarize our findings and present some concluding remarks.

II. EXPERIMENTAL SETUP

The data were obtained using a 0.2 nA_e 35 MeV per nucleon ^{40}Ca beam at the SARA (Système Accélérateur Rhône-Alpes, Grenoble, France) facility. The self-supporting 50 $\mu g/cm^2$ natural copper target was located inside the AMPHORA multidetector. AMPHORA (Fig. 1) is a 140 detector CsI array which covers 82% of 4π *sr*. The 48 detectors of the forward wall lie on a honeycomb frame at a distance of 1.40 m from the target. The backward ball is arranged into seven rings comprising in all 92 trapezoidal detectors with distances ranging from 0.12 to 0.44 m from the target. The forward-angle detectors (angles ranging from 2° to 57° in the laboratory frame) were equipped with thin (100 to 200 μm) Bicron BC400 plastic foils. The identification of light particles in charge ($Z=1$, 2, and 3) and mass was made by the CsI(Tl) crystals (Fig. 2). For those detectors equipped with plastic foils, the identification of heavier fragments (up to $Z=20$) was possible (Fig. 3). In both cases, particle identification was made using pulse shape analysis. Isotopic separation is obtained in all detectors from $Z<3$ and unambiguous identification of the charge of detected fragments in the plastic foil+CsI detectors for $Z\leq 9$. For higher charges, no such clear separations are observed. However, we were able to make charge identification in this region using a semiautomatic masking procedure [18] with estimated uncertainty of ± 1 charge unit in most cases and less than ± 2 units in all cases. The identification consisted of a global manual adjustment of a set of curves which coincide with the crests of the clouds connected with each charge, using five tuning parameters. The separation between the crests was fixed by a progression law based on energy loss. For charges $Z\leq 9$, the adjustment was unambiguous. For higher charges, the progression law has been supplemented using the elastic $Z=20$ cloud at most forward angles and odd-even effects for other rings.

It has been shown that the particle incident energy is

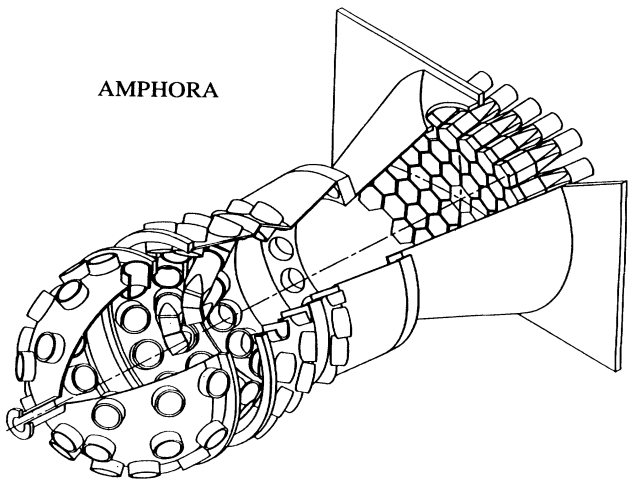

FIG. 1. Schematic view of the multidetector AMPHORA. The forward wall is composed of 48 CsI detectors equipped with 200-μm plastic scintillators. The ball is composed of 92 CsI detectors of which the three forward rings are equipped with 100-μm plastic foils.

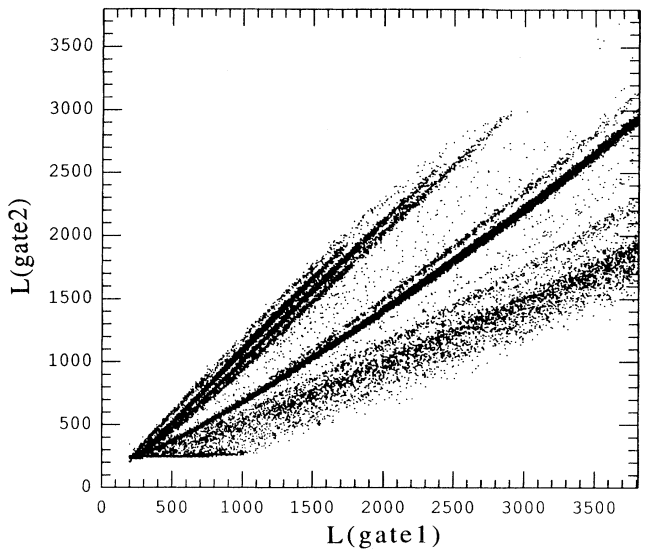

FIG. 2. Typical identification map for CsI detectors (see text). Ions with $Z<3$ are identified in mass as well as in charge.

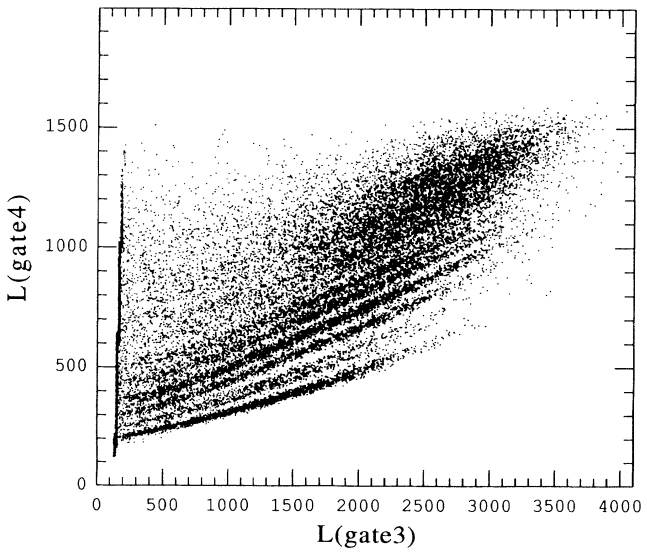

FIG. 3. Typical identification map for plastic+CsI detectors. Ions with $Z\leq 9$ are clearly identified. Identification of higher charges is based on a semiautomatic masking procedure (see text).

proportional to the integration, in a 400 ns gate, of the light deposit in the CsI crystal when acting alone [19]. Hence, a few calibration points (thorium source, alpha-particle calibration beam, stopping energies) are sufficient to allow an energy calibration to within a ±5% error [20]. For plastic foil+CsI detectors the calibration was made via published calibration parameters [21], with uncertainties of 3.5%, 5%, and 6.5% at 2, 8, and 15 MeV per nucleon, respectively.

The identification thresholds were imposed by the thicknesses of the plastic foils, which were 100 μm for the rings set at 31° and 47° and 200 μm for the more forward detectors. In this latter case, the thresholds reach 3.6 MeV for protons, 14.2 MeV for alpha particles, and, approximately, 7 MeV per nucleon for heavier particles.

III. EVENT SELECTION

In this work, we concentrate mainly on the analysis of quantities derived from the charge partition weights $W(n_1,n_2,\ldots,n_{Z_{\rm tot}})$, where n_k is the number of fragments of charge k and $Z_{\rm tot}$ is the total charge. Most analyses of charge partitions (multinomial method [22], intermittency [23], charge moments [24]) require an event sample corresponding to the disintegration of a well defined parent nucleus measured with close to 100% efficiency. This is, of course, due to the fact that even some quite simple global variables may suffer some distortion due to the rejection of incompletely detected events [25]. Thus, in the present study, we focus on peripheral and midperipheral collisions for which the fragments resulting from the decay of excited PPLF's have energies well above the detector thresholds whereas only some few light particles from the PTLF (primary target-like fragment) are detected.

It was necessary to identify the source of every detected particle in order to isolate a sample of completely detected quasiprojectile disintegrations. This was achieved essentially by an event-by-event determination of the frame of reference in which the PPLF, prior to disintegration, is motionless (c.m. frame). The procedure employed involves three steps.

Since slow moving target-like fragments produced in peripheral collisions are expected to remain undetected, a first evaluation was made by calculating the c.m. of all the particles with charge $Z \geq 3$. Already at this stage, projectilelike and targetlike sources are clearly visible and it was observed that, in the selected sample of events, very few lithium nuclei, and no particles with $Z > 5$, are evaporated from the PTLF nuclei, thus providing some *a posteriori* justification for the choice of the $Z = 3$ cutoff. A more accurate evaluation was then made by retaining only the particles with charge $Z \geq 3$ which were included in a velocity selection sphere centered on the first calculated c.m. in velocity space. The radius of the sphere was set to $v = 0.45 v_{beam}$ so as to include all particles emitted in the forward direction. In a third step, this process was repeated including $Z = 1$ and $Z = 2$ particles for which the appropriate velocity radii were $0.6 v_{beam}$ and $0.5 v_{beam}$, respectively. Finally, 150 000 events for which the total charge assigned to the PPLF was $Z_{\rm tot} = 20$ were selected. The set of events can thus contain PPLF's which have picked up some nucleons from the target, the corresponding excess charge being not detected. In fact, simulations show that, thanks to the motion of the center of mass of the particles and to the good angular coverage of AMPHORA, such events are scarce. *In the following, unless explicitly mentioned, we will deal only with this sample of* $Z_{\rm tot} = 20$ *events.*

As the center of mass of the PLF is known, it is possible to represent the velocity vectors in this reference frame. Figure 4 presents the observed alpha-particle distribution (each point represents one alpha particle) obtained in this way. One can clearly see the Coulomb barrier effect around the center of mass of the parent nucleus. The dark ring corresponds to the particles emitted by the PPLF whereas the cloud (which contains only about 10% of the alpha particles) corresponds to the other sources (PTLF, preequilibrium). The fact that the Coulomb circle is almost empty shows that there is very little contamination of the set of alpha particles assigned as PLF's coming from other sources (less that 7%). A similar picture is obtained for protons (15% target contamination). For higher-charge particles, we obtain a perfect separation between the projectilelike and target-like fragments. Thus the selection seems reliable. Detected intermediate mass fragments and heavy residues originate exclusively from the quasiprojectile. Some light particles emitted from the PTLF, which are detected in the forward direction may just compensate undetected PLF's, but such events should be scarce.

A. Effect of detection efficiency

It is known that, for AMPHORA [16] and other such 4π multidetectors, the detector response function may

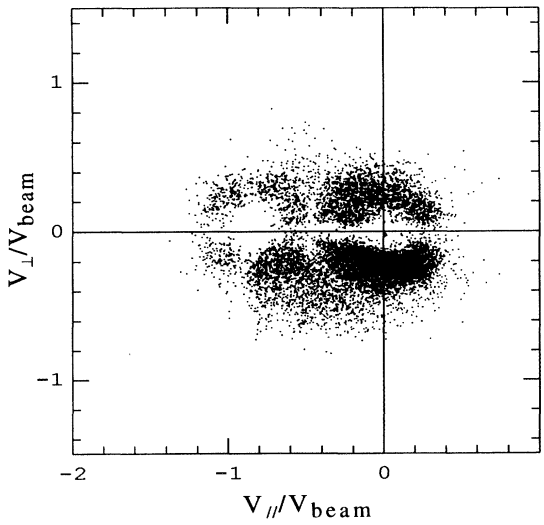

FIG. 4. Distribution of α-particle velocities in the reference frame centered on the (reconstructed) projectilelike fragment velocity. The horizontal axis in this plot coincides with the PPLF-PTLF relative velocity.

severely distort certain global variables [25,26]. This response function is essentially due to two factors: the geometrical efficiency (in AMPHORA, one-sixth of the 4π space is not covered by detectors and another sixth, at 90°, is shadowed by the target holder), and the thresholds. Nevertheless, the velocities of the fragments emitted by the PPLF's are much higher than the detector thresholds even if the fragment is emitted backward to the PPLF direction. Moreover, the PPLF fragments are focused in the high-granularity forward direction of the multidetector. Furthermore, simulation studies [25] indicate that, essentially due to the high forward-angle granularity of AMPHORA, geometric effects do not seriously impair the detection of PLF's.

B. Event-by-event total energy balance

The total energy of the system is 1400 MeV. This energy is shared between the PPLF and the PTLF.

The PPLF total energy is made up of the kinetic energy of its center of mass, the kinetic energies of the charged fragments in its center of mass, the Q value for the disintegration, and the kinetic energy of the unobserved neutrons. The first two terms are directly measured. The latter ones have been evaluated with a simulation code. A large number of disintegrations, for various excitation energies and angular momenta, have been simulated by the Monte Carlo evaporation code BINFRAG [27]. For each event, the charge and mass partitions, as well as the Q value, were stored in such a way as to construct a neutron-number spectrum (and corresponding Q-value spectrum) for each charge partition. Hence, it was possible to affect an average Q value and an average number of neutrons to each experimental event. A first evaluation of the temperature (T_1) is made assuming a kinetic energy of 10 MeV per neutron and assuming the relation $E_1^* = (A/8)T_1^2$. The value of E_1^* is obtained by summing the Q value and the kinetic energies of the charged particles and the neutrons. The final kinetic energies of the neutrons are fixed to $2T_1$. The final excitation energy E^* is then calculated using this value of the neutron kinetic energy. The total neutron contribution is, on average, 12% of the PPLF excitation energy.

The position of the PTLF in the velocity space can be deduced from that of the PPLF using momentum conservation. The excitation energy of the PTLF is obtained by fitting PTLF light evaporated particle spectra in its rest frame for subsets of events belonging to the same PPLF excitation-energy region. The sum of the kinetic and excitation energies of the two primary fragments gives the event-by-event total energy (Fig. 5). The calculated total energy spectrum shows a Gaussian shape which is centered at 1350 MeV, close to the total entrance-channel energy (1400 MeV). This can be considered as evidence that the energy calibrations do not suffer from any significant systematic error. The width of the spectrum ($\sigma = \pm 10\%$) is mostly due to the difficulty of measuring correctly the kinetic energy of the PPLF, which is the dominant term in the sum, due to the uncertainties of the detector calibration (see Sec. II). The relative error for the excitation energy of the PPLF is about $\pm 10\%$.

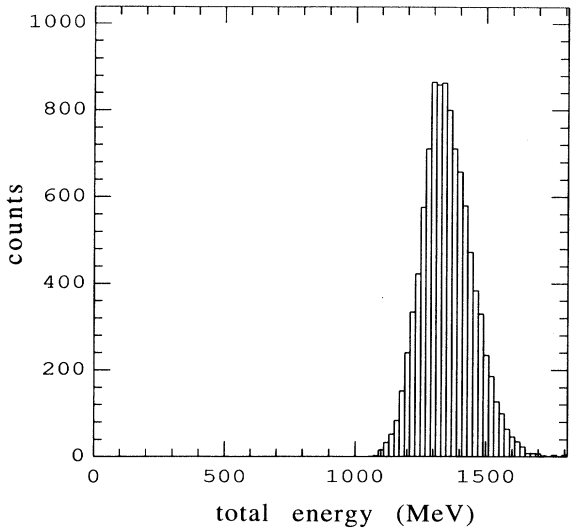

FIG. 5. Total reconstructed energy spectrum obtained by summing the kinetic and excitation energies of the PTLF and the PPLF and measuring the temperature of the PTLF by fitting light evaporated particles in subsets of events.

IV. INTERMEDIATE-MASS FRAGMENT EMISSION

Important features of the event sample can be seen in Fig. 6 which shows the charge of each fragment plotted against the event excitation energy. Each point stands for one particle. The dark zone at the bottom of the map corresponds to hydrogen and helium nuclei, which are about ten times more numerous than lithium in the whole excitation energy domain. At very low excitation energy, events consist of one $Z = 20$ particle (elastic or inelastic scattering). For higher energies (evaporation domain) light particles are detected together with a heavy residue. The first intermediate-mass fragments appear at an excitation energy of 50 MeV. The intermediate-mass frag-

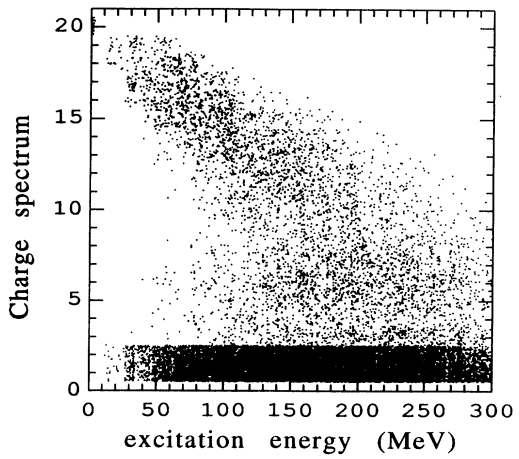

FIG. 6. Distribution of PLF charge as a function of excitation energy of the event. Each plotted point corresponds to one charged particle. At the lowest energies only evaporative processes are visible whereas at the highest energies the decay produces only light particles and intermediate mass fragments.

ments (IMF's) will be defined herein as fragments with charge between 3 and 11, so that if there are three (or more) IMF's there can be no heavy residue with charge strictly superior to 11. One interesting first result can be seen in Fig. 7(b), which shows the probability for an event to include 0, 1, 2, 3, or 4 IMF's as a function of the excitation energy. The events containing two IMF's correspond either to fissionlike decays or to the evaporation of two lithium nuclei. The three-IMF-event threshold is 2.5 MeV per nucleon. This value is low compared with the predictions of many models for the threshold of multifragmentation [6,28]. A similar low value was also observed by Hu on a heavier system [29]. It would thus be unwise to consider three-IMF observation as a signature [30] for the approach of a phase transition (see Suraud *et al.* [1] for a discussion of this point). Figure 8 are scatter plots of the correlation between the three largest fragments ($Z_1 \leq Z_2 \leq Z_3$) in each event. In these plots, the horizontal axis corresponds to the difference $z_2 - z_1$ and the vertical axis to the difference $z_3 - z_2$ where $z_i = Z_i/(Z_1+Z_2+Z_3)$. Every event falls into a right-angled triangle, the horizontal edge of which represents the events with two equal largest fragments, while the vertical edge represents the events with two equal second largest fragments, and the hypotenuse represents the events with multiplicity $M=2$. We define evaporative events as having one heavy fragment $Z_3 \geq 11$ and the other two with charge $Z_1, Z_2 \leq 3$. They mostly lie in the top apex [circles in Fig. 8(a)]. The fissionlike events (two fragments with charge $Z_2, Z_3 \geq 7$ and the third with charge $Z_1 \leq 3$) lie in the right apex (squares). Defining, as above, multifragment events as those containing three IMF's we find that they are localized in the left apex (plus signs). Finally, the vaporization events ($Z_3 \leq 2$) lie on three points close to the origin (crosses). The fissionlike threshold is 50 MeV. Unlike the results published in Ref. [31], the data show no sudden evolution at any given excitation energy.

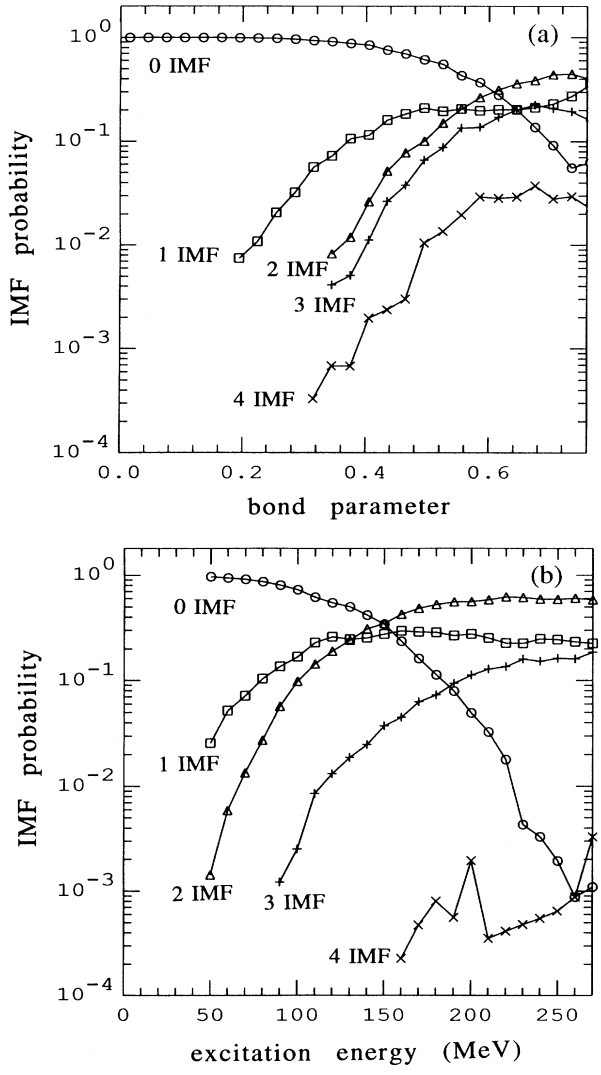

FIG. 7. Evolution of the probability of observation of intermediate mass fragments (fragment with charge included between 3 and 11). Circles: 0 IMF, squares: 1 IMF, triangles: 2 IMF, plus signs: 3 IMF, crosses: 4 IMF. (a) Evolution with percolative bond parameter in percolation model. (b) Corresponding plot for the physical events as a function of the excitation energy.

V. COMPARISON OF CHARGE MOMENTS WITH THE PERCOLATION MODEL

A. Analogy between physics and the percolation model

For many experiments, percolation simulations have been shown to be able to reproduce several features of the

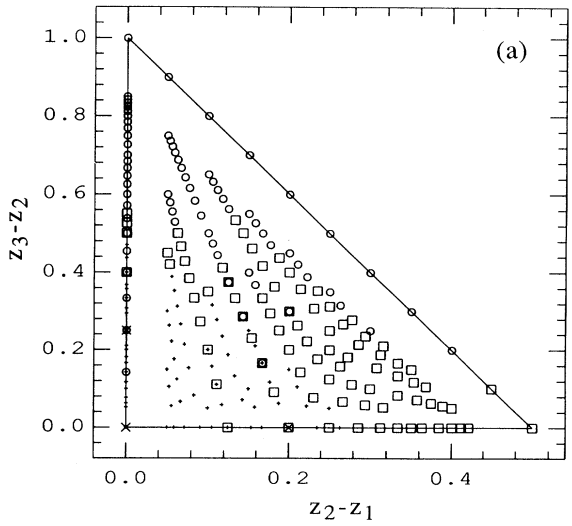

FIG. 8. Dalitz plots of the three largest fragments in an event ($Z_3 \leq Z_2 \leq Z_1$), $z_i = Z_i/[Z_1+Z_2+Z_3)]$: (a) representation of all the 627 possible partitions: the open circles represent evaporationlike events ($Z_3 \geq 11$), the squares quasifission ($Z_2 \geq 7$, $Z_1 \leq 3$), the plus signs multifragment events ($Z_1 \geq 3$, $Z_3 \leq 11$), and the crosses vaporization events ($Z_3 \leq 3$); (b) experimental data for various energy bins; the horizontal and vertical scales are the same as in (a).

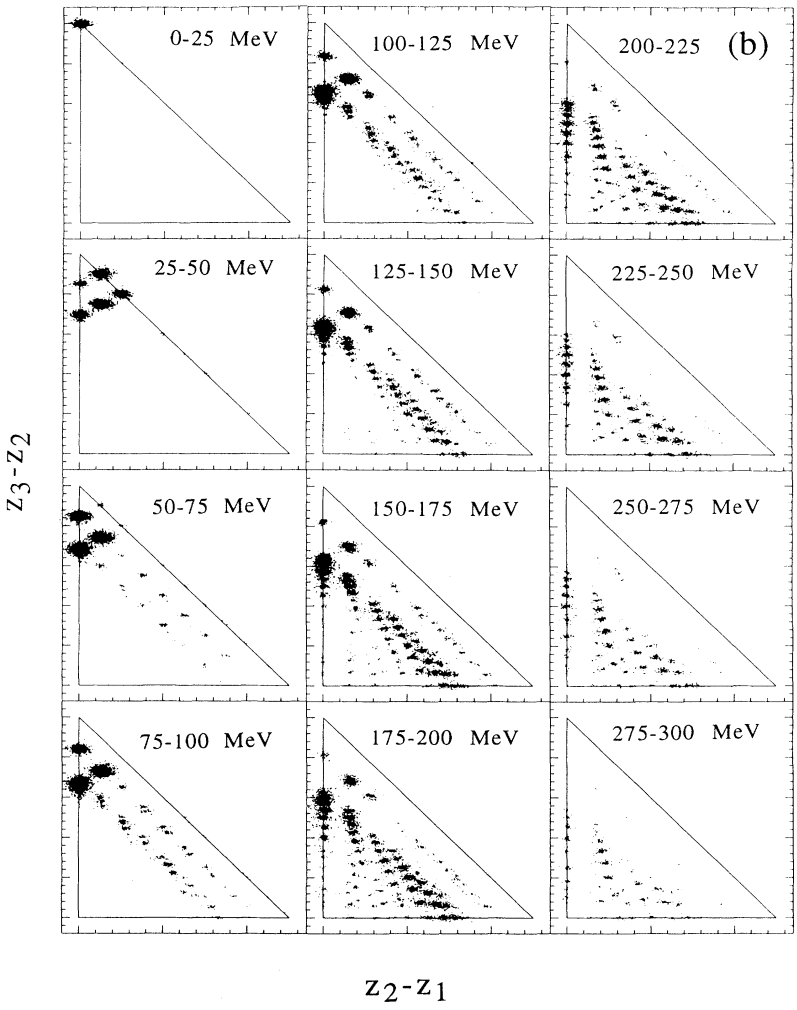

FIG. 8. (*Continued*).

experimental charge distributions [31]. This is perhaps surprising since these simulations contain neither the dynamics nor the structure information which are usually considered to be essential ingredients of nuclear decay models. Our first goal will therefore be to check to what extent this feature is preserved for systems as small as calcium and to investigate the behavior of the physical events corresponding to bond-breaking parameters p close to the critical value p_c. These physical events will be called "critical" events even if one should be aware of the fact that this denomination only means that they correspond to percolation events which are in the critical region.

The percolation crystal used is a simple cubic frame with 20 sites arranged in such a way as to produce the most compact structure. The charge moments ([24], see below) of order greater than or equal to 2 reach a smooth maximum for bond-breaking parameters near $p_c = 0.65$.

In order to make a comparison between our event sample and percolation it is necessary to select events corresponding to the same pseudotemperature (p is the image of the nuclear temperature). For this we need to establish a link between the excitation energy of physical events E^* and the bond-breaking parameter of percolative events. As both E^* and p are well correlated with the multiplicity, we have associated the mean values $\langle E^* \rangle_M$ and $\langle p \rangle_M$ obtained for each value of the multiplicity (Fig. 9). The maximum experimental multiplicity is $M = 13$. The interpolation of the curve between the thirteen points gives a correspondence for excitation energies ranging from 0 to 350 MeV and for bond-breaking parameters ranging from 0 to 0.75. It will be noted that this interval includes the critical bond parameter.

The preceding method gives a one-to-one relation between p and E^*. We have also discovered an iterative method which makes it possible to generate a bond-breaking probability distribution is such a way as to create a sample of percolative events which reproduces the physical multiplicity spectrum.

We first divide the full range of bond-breaking parameters, [0,1], into n bins. We denote by $P(i)$ the probability that the bond parameter p belongs to the range $[(i-1)/n, i/n]$, $P(m)$ the probability that the multiplicity $M = m$, and $P(A|B)$ the conditional probability of A given B. The index φ stands for physical data and the index k is the number of the iteration. With these notations, the inputs of the procedure are the conditional percolation multiplicity probabilities $[P(m|i)]$ and the phys-

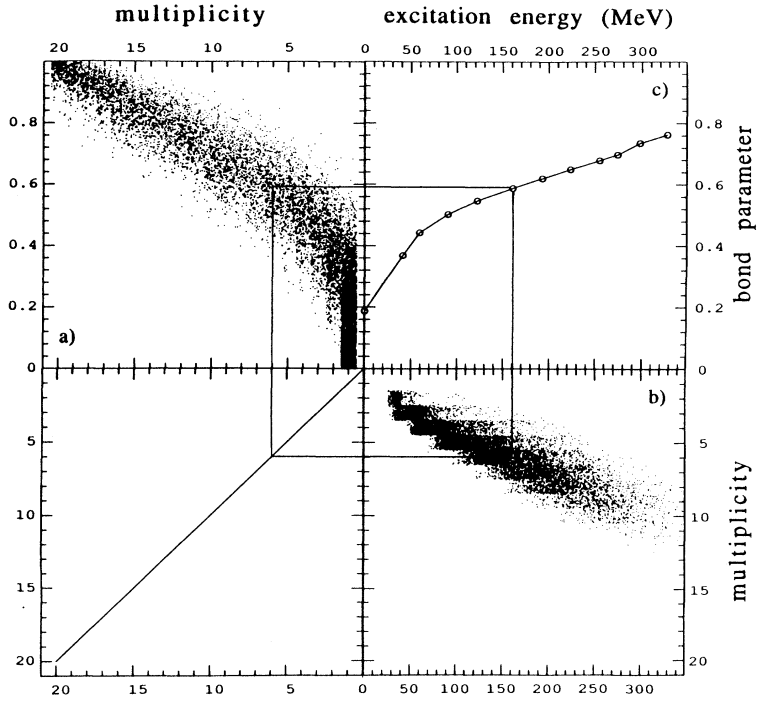

FIG. 9. Correspondence between excitation energy and bond probability: (a) correlation map between bond probability and multiplicity for percolative events, (b) correlation map between excitation energy and multiplicity for percolative events, (c) correlation map between p and E^* obtained by associating the mean values of these parameters for each multiplicity.

ical multiplicity spectrum $[P_\varphi(m)]$.

We define an iterative procedure

$$P_k(i)=\sum_m P_\varphi(m)P_{k-1}(i|m) \tag{1}$$

where, for large k, $P_k(i)$ should converge to the required bond parameter spectrum.

Using

$$P(A|B)=\frac{P(B|A)P(A)}{P(B)}$$

(1) can be rewritten

$$P_k(i)=\sum_m P_\varphi(m)\frac{P_{k-1}(m|i)P_{k-1}(i)}{P_{k-1}(m)} \ . \tag{2}$$

We also have

$$P_{k-1}(m)=\sum_{i'} P_{k-1}(i')P_{k-1}(m|i') \ . \tag{3}$$

Due to the fact that $P_{k-1}(m|i)$ does not depend on the distribution $P(i)$, (2) can finally be written as

$$P_k(i)=P_{k-1}(i)\sum_m \frac{P_\varphi(m)P(m|i)}{\sum_{i'} P_{k-1}(i')P(m|i')} \ . \tag{4}$$

The iterative procedure represented by Eq. (4) is terminated when the resulting multiplicity spectrum (3) is the same as the physical one $P_\varphi(m)$, to within the numerical precision.

The bond parameter distribution (4) obtained is much narrower than the corresponding experimental excitation-energy distribution. This is due to the fact that the correlation of the multiplicity with E^* is stronger than with p. Nevertheless, the corresponding percolative sample of events can directly be compared with the experimental data.

B. Charge moments

The comparison between the physical data and the percolation model is made via the charge-moment analyses as introduced by Campi [24]. The reduced charge moment of order k is given by

$$M_k=\frac{\sum_i Z_i^k}{Z_{\text{tot}}}$$

where the sum runs over all the fragments excluding the heaviest one. $M_0=(\text{multiplicity}-1)/Z_{\text{tot}}$ is the reduced multiplicity.

The first plot [Figures 10(a) and (b), where each point stands for one event] shows the correlation between the largest fragment of the event and the reduced multiplicity for the percolative and the physical samples of events. The percolation events have been generated using the technique described above. The spectra are similar. On the same plots, a histogram gives the evolution of the variance of the greatest charge. The maximum of each histogram is attained for the same multiplicity ($M=6$). The fluctuation of the charges in a given event is displayed in Fig. 11. The γ_2 value is a combination of the charge moments $[\gamma_2=M_0M_2/M_1^2=1+\sigma^2(Z)/\langle Z\rangle^2]$. Both in the physical events and in the percolation events one obtains large charge fluctuations ($\gamma_2>2$). The averaged values represented by histograms show similar behavior.

As mentioned earlier, a correspondence has been established between p and E^* and we know the critical value

of p. Hence we are able to select percolation events close to the critical point ($E^* \in [190,210]$ MeV) and the physical events in the corresponding excitation-energy range. For the subset of data, we plot $\ln(S_3)$ versus $\ln(S_2)$ with $S_i = M_i / M_1$ (Figure 12 where each circle stands for one partition, the surface being proportional to the number of events belongs to the partition). The fit of the plots with straight lines gives the slopes $\lambda_{3/2}$ for percolation and physical events. The value of $\lambda_{3/2}$ is related to the value of the so-called critical exponent τ by the relation $\tau = (3\lambda_{3/2} - 4)/(\lambda_{3/2} - 1)$. We obtain $\tau = 2.14$ (percolation) and $\tau = 2.10$ (data), which are quite close. The value obtained from mean-field theory [32] is rather greater (~ 2.33). One can also notice that, for $Z_{\text{tot}} = 20$, both the critical probability ($p_c \approx 0.65$) and the critical energy ($E^* \sim 200$ MeV) correspond to the crossover of the 0 IMF and 3 IMF probability curves (see Fig. 7).

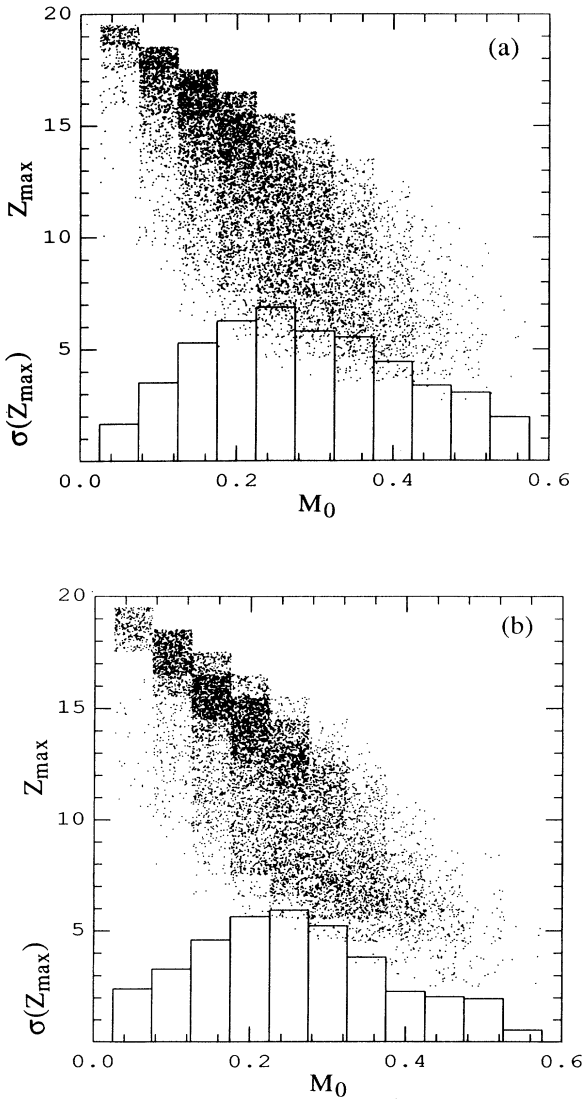

FIG. 10. Plot of maximum charge Z_{max} versus reduced multiplicity M_0 (a) for percolation and (b) for physical events. The histograms represent the standard deviations of the Z_{max} distributions. The similarity between the percolation and physical events is obvious.

C. Preliminary conclusions

For simple moments of the charge distribution the percolation simulation gives results which are in good agreement with experiment. It appears that we can select events which are close to the critical point (by analogy with percolation). This critical zone corresponds to excitation energies in the range 190 to 210 MeV, that is, excitation energies per nucleon close to 5 MeV per nucleon.

D. Nonaveraged charge moments

As seen previously, the percolation model is able to reproduce the behavior of many averaged physical observables. This is true not only close to the "critical" point but for the whole excitation-energy range. It is then of interest to seek for differences by investigating the

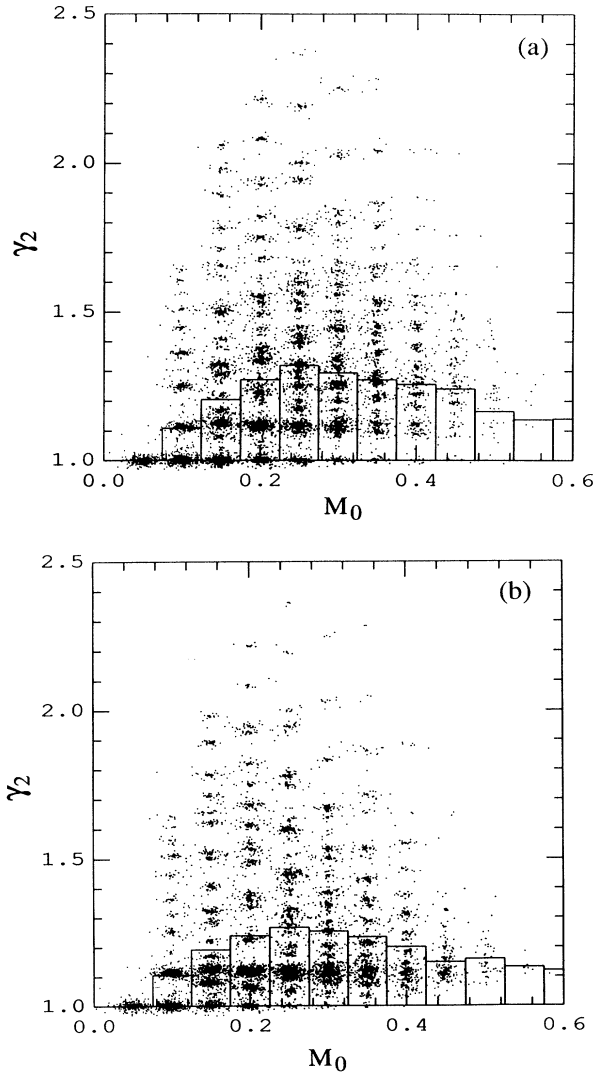

FIG. 11. Same as Fig. 11 for the charge moment γ_2 (see text).

details of these distributions when the moments are not averaged. In order to do this, Jaqaman *et al.* [33] have proposed to plot the correlation map between $\ln(S_2)$ and $\ln(Z_{max})$, where Z_{max} is the largest fragment in the event. The comparison of the results for percolation and a microcanonical Metropolis sampling calculation [12] shows a relative depreciation in the upper-right zone of the former. This zone corresponds to the pseudofission events, i.e., in the present case, events with exactly two fragments with charge greater than 5. This study has been made for nuclei much larger than calcium (64 sites for percolation, 79 protons for the fragmentation code). The lack of pseudofission in the percolation simulation was explained by the fact that it includes only short-range links between neighboring nucleons whereas the long-range Coulomb forces where included in the microcanonical simulation code.

We have performed the same kind of comparison between our data and the corresponding percolation data set. The resulting correlation maps can be seen in Figs. 13(a) and 13(b) where each circle corresponds to a charge partition, the surface being proportional to the number of events belonging to the partition. The plots are quite comparable even (by opposition to the Jaqaman *et al.* result) in the pseudofission zone. This may be due to the fact that the role of the Coulomb force is less important for small systems. This conclusion is corroborated by the spectrum displaying the probabilities for an event to include 1, 2, 3, or 4 IMF's (Fig. 7). The pseudofission curve ($n_{IMF}=2$) shows similar behavior for the percolation and the physical events. The correlation map also shows that, apart from vaporization, the sample contains events be-

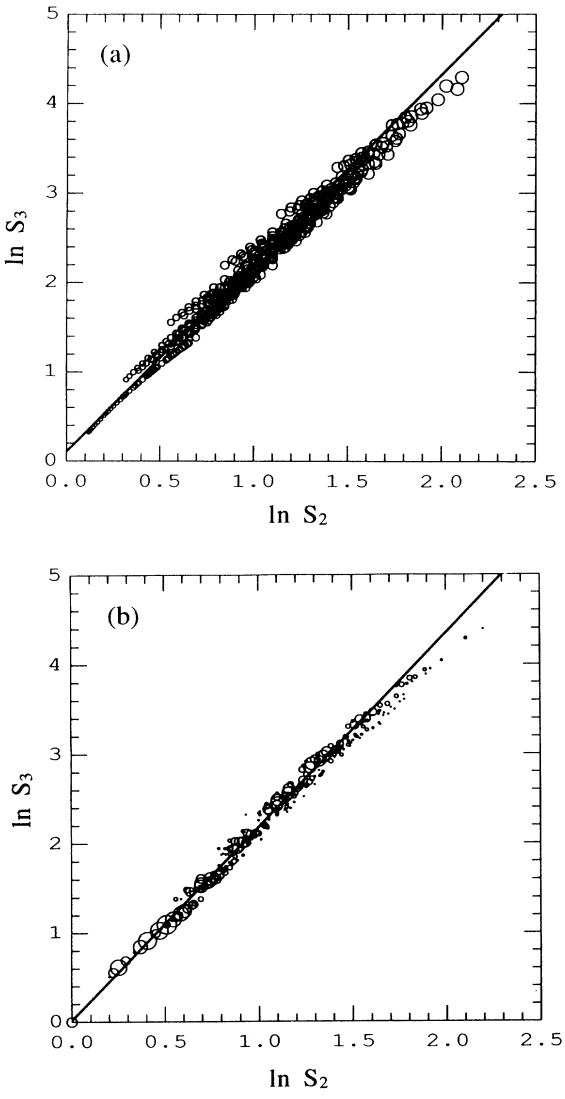

FIG. 12. Comparison of the plots of charge moments S_3 versus S_2 (a) for percolation and (b) for the physical event sample. The slopes of these plots are related to critical indices as explained in the text.

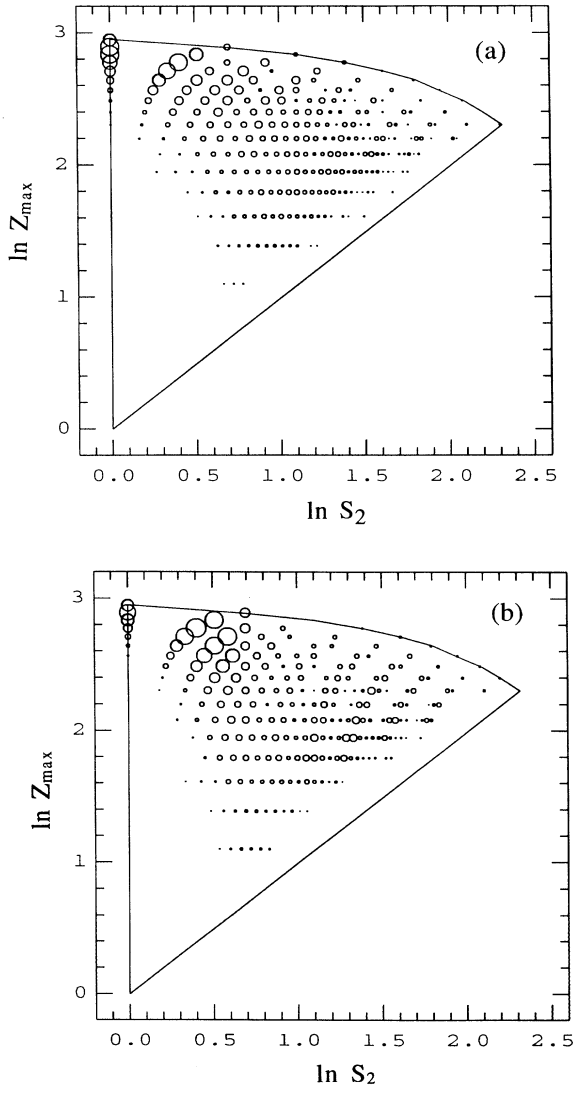

FIG. 13. Correlation between $\ln(S_2)$ and $\ln(Z_{max})$ where $S_2=M_2/M_1$ and Z_{max} is the largest fragment in the event. Each partition is represented by a circle, the surface of which is proportional to the number of events belonging to the partition: (a) for percolative events, (b) for physical data.

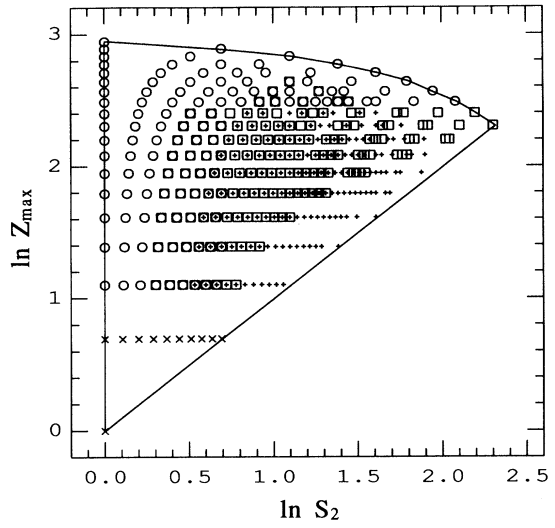

FIG. 14. Representation of all partitions in the form of Fig. 13. As in Fig. 8(a), the open circles represent evaporation-like events, the squares quasifission (2 IMF), the plus signs cracking events (≥ 3 IMF) and the crosses vaporization events (0 IMF and no large residue).

longing to the evaporative, pseudofission, and multifragment emission (MFE) domains. This can be seen by comparing with Fig. 14 where the circles correspond to evaporative events ($n_{\mathrm{IMF}} \leq 1$, one heavy residue), the squares to pseudofission ($n_{\mathrm{IMF}}=2$), the plus signs to MFE ($n_{\mathrm{IMF}} \geq 3$), and the crosses to vaporization ($n_{\mathrm{IMF}}=0$, no heavy residue). Some partitions are much more populated in the experimental sample than in the percolation one. They are arranged along almost vertical lines on the map. They correspond to the differential stability of certain physical particles as compared with the particles

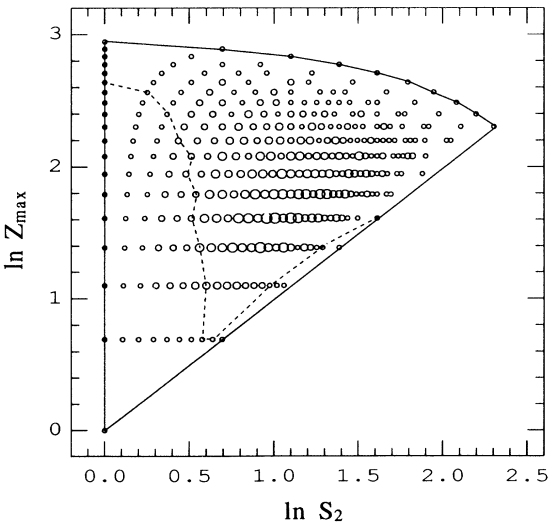

FIG. 15. Pseudo phase space, representation of all partitions. Larger circles are drawn when several partitions lie on the same point. The dashed line approximately divides the figure into two regions, in the upper one the Q value is less than 100 MeV.

generated by the percolation model. Alpha particles and carbon nuclei are most abundant in the physical sample. This abundance is compensated by the fragments with one, three, four and nine charges in the percolative sample. The density of the events in the plot seems to be also influenced by the partition Q values. Only the partitions corresponding to Q values which are lower than about 100 MeV are populated (Fig. 15). In the phase-transition description, the critical events are those with large values of S_i ($i \geq 2$). Here these events lie on the right side of the map. The sample contains events with the largest possible values of S_2.

From the correlation map, the so-called critical exponent τ can be extracted. The values obtained for the physical sample and the percolation simulation are respectively $\tau=2.10$ and $\tau=2.17$.

VI. SEARCH FOR A CHANGE IN THE DISINTEGRATION MECHANISM

The analysis in terms of charge moments of the sample of physical events shows that it includes subcritical and overcritical events, the critical point being reached for an excitation energy of about 5 MeV per nucleon. The problem is to know if this point actually corresponds to a change of disintegration mechanism. No indication of such a change can be seen on the Dalitz charge plots of Fig. 8(b).

An independent signature is to be found in the dynamical variables. The shape of the emission in the momentum space can be characterized by the momentum tensor variables:

$$T_{ij}=\frac{\sum_{n=1}^{M} P_{ni}P_{nj}/|P_n|}{\sum_{n=1}^{M}|P_n|} .$$

In this equation i and j are two of the three directions in momentum space, n is the number of the fragment, M the multiplicity, and P_n the momentum of the particle in the reference frame of the parent nucleus. The three eigenvectors of this tensor give the three principal axes of the ellipsoid characteristic of the emission. The eccentricity $\mathcal{E}$ measures its isotropy, $\mathcal{E}=[q_3-\frac{1}{2}(q_1+q_2)]/(q_1+q_2+q_3)$, where the q_i are the square roots of the eigenvalues, q_3 being the more different of the three. If the emission is isotropic (which may be expected for very explosive events), the ellipsoid will be a sphere and $\mathcal{E}=0$. For a prolate shape (pseudofission) $\mathcal{E}\in[0,1]$ and, for an oblate shape, $\mathcal{E}\in[-\frac{1}{2},0]$ (in-plane emission).

The inclusive analysis of the eccentricity as a function of the excitation energy can lead to biased conclusions. Indeed, at low excitation energy, one can only have events with multiplicity 2 ($\mathcal{E}=1$) or 3 ($\mathcal{E}=-\frac{1}{2}$). As the excitation energy increases, the mean multiplicity also increases, and the value of $\mathcal{E}$ can approach zero. Hence the evolution is mostly governed by the charge distribution and only slightly by the disintegration dynamics. In order to get rid from this effect, the [excitation energy, eccentricity] correlation has been studied for fixed values of

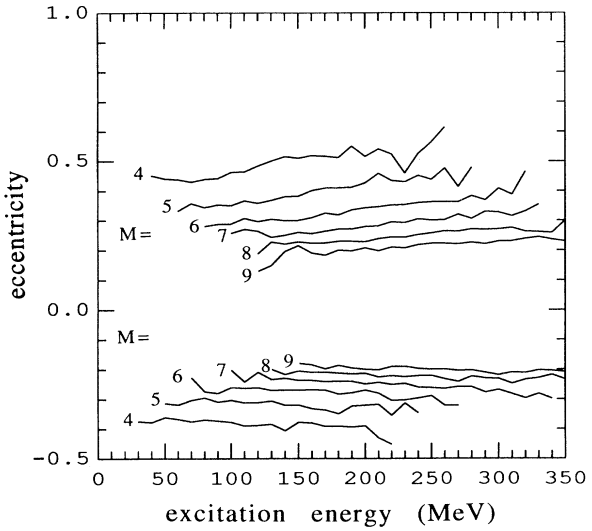

FIG. 16. Variation with excitation energy of the momentum ellipsoid average eccentricities for physical events with fixed multiplicity M. The upper group of curves represents prolate shapes whereas lower group corresponds to oblate shapes.

the multiplicity. The averaged values of eccentricity, for oblate and prolate events and for different multiplicities, are shown in Fig. 16.

Different observations can be made concerning these spectra: (i) As stated earlier, the sphericity increases with the value of the multiplicity. (ii) For a given multiplicity, the sphericity decreases as a function of the excitation energy. Though the effect is not very strong, it is constant and systematic over the multiplicities. It can be explained by an angular-momentum effect. The events with higher excitation energies correspond to increasing angular momentum so that emitted fragments tend to be focused more and more in the reaction plane. The focusing effect of the rotational motion apparently increases faster than the defocusing effect due to the thermal (isotropic) part of the excitation energy. (iii) From our data it is clear that no signal for a change in mechanism can be seen in the critical region. The same conclusion can be drawn from the nonaveraged plots: the clouds corresponding to events with a fixed multiplicity or a fixed number of IMF's show no substructure which could have been caused by different reaction mechanisms.

VII. SUMMARY AND CONCLUSIONS

We have presented in this work a data sample obtained by reconstructing primary projectilelike fragments in quasibinary collisions of 35 MeV per nucleon ^{40}Ca with a ^{nat}Cu target. From this sample 150 000 events corresponding to the projectile charge were isolated and analyzed.

The analysis was mainly concerned with quantities obtained from charge partitions and the corresponding weights. It was shown that certain derived quantities (e.g., the charge moments) vary with the PPLF excitation energy in a way which is quite comparable with the variation of the same quantities with the bond parameter in a simple percolation simulation. In particular, by establishing a correspondence between PPLF excitation energy and the percolation bond parameter, it was shown that the data-sample excitation energy spectrum, which extends up to 7.5 MeV per nucleon, contains a critical region (in the percolation sense) close to 5 MeV per nucleon lying above the threshold for production of three intermediate mass fragments. Value of the critical exponent, found for percolative and physical events, are very similar.

A more refined (iterative) technique was presented which leads to the construction of a bond-parameter spectrum which reproduces the global experimental multiplicity spectrum. In this case, the main features (including pseudofission events) of the experimental charge partition spectrum are reproduced by the simulation.

Analysis of momentum ellipsoids was carried out as a function of excitation energy. Strong effects were observed due to in-plane focussing associated with angular momentum transferred to the PPLF. These effects become stronger as the excitation energy increases. However, no evidence for a change in disintegration mechanism was obtained. This finding agrees with an earlier analysis of heavy-fragment recoil effects [34] and casts doubt on the usefulness of investigations of charge partitions or their moments in the search for prompt multifragmentation. In one sense, the comparison of the data with the percolation simulation supports this conclusion since in the latter case the passage through the critical region cannot be associated with dynamical effects in the disintegration mechanism. On the other hand, we feel that a fuller investigation of angular-momentum effect in the multifragmentation mechanism should be carried out before definite conclusions may be drawn.

[1] E. Suraud, Ch. Grégoire, and B. Tamain, Prog. Part. Nucl. Phys. **23**, 357 (1989).
[2] D. H. E. Gross, Rep. Prog. Phys. **53**, 605 (1990).
[3] G. F. Bertsch and S. Das Gupta, Phys. Rep. **4**, 189 (1989).
[4] B. Remaud, C. Gregoire, F. Sebille, and P. Schuck, Nucl. Phys. **A488**, 423C (1988).
[5] E. Sureaud, M. Pi, P. Schuck, B. Remaud, F. Sebille, C. Gregoire, and F. Saint-Laurent, Phys. Lett. B **229**, 359 (1989).
[6] S. Levit and P. Bonche, Nucl. Phys. **A437**, 426 (1985).
[7] T. D. Thomas, Annu. Rev. Nucl. Science **18**, 343 (1968).
[8] L. G. Moretto, Nucl. Phys. **A247**, 211 (1975); W. A. Friedman and W. G. Lynch, Phys. Rev. C **28**, 16 (1983).
[9] B. Borderie, Orsay Report No. IPNO-DRE-92-03.
[10] R. Bougault, J. Colin, F. Delauney, A. Genoux-Lubain, A. Hajfani, C. Le Brun, J. F. Lecolley, M. Louvel, and J. C. Steckmeyer, Phys. Lett. B **232**, 291 (1989).
[11] A. J. Cole, N. Longequeue, J. Menet, J. J. Lucas, R. Ost, and J. B. Viano, Nucl. Phys. **A341**, 284 (1980); F. Puhlhofer, *ibid.* **A280**, 207 (1977); J. Richert and P. Wagner, *ibid.* **A517**, 399 (1990); R. Charity, M. A. McMahan, G. J. Wozniak, R. J. McDonald, L. G. Moret-

to, D. G. Sarantites, L. G. Sobotka, G. Guarino, R. Pantaleo, L. Fiore, A. Gobbi, and K. D. Hildenbrand, *ibid.* **A483**, 371 (1988).

[12] Zhang. Xiao-Ze, D. H. E. Gross, Xu Shu-Yan, and Zheng Yu-Ming, Nucl. Phys. **A461**, 668 (1987); S. E. Koonin and J. Randup, *ibid.* **A474**, 173 (1987); J. P. Bondorf, R. Danangelo, I. N. Mishustin, C. J. Pethick, H. Schulz, and K. Sneppen, *ibid.* **A443**, 321 (1985).

[13] R. T. De Souza, N. Carlin, Y. D. Kim, J. Ottarson, L. Phair, D. R. Bowman, G. K. Gelbke, W. G. Gong, W. G. Lynch, R. A. Pelak, T. Peterson, G. Poggi, M. B. Tsang, and H. M. Xu, Nucl. Instrum. Methods **A295**, 109 (1990).

[14] J. Hubele, P. Kreutz, J. C. Adloff, M. Beremann-Blaich, P. Bouissou, G. Imme, I. Iori, G. J. Kunde, S. Leray, V. Lindenstruth, Z. Liu, U. Lynen, R. J. Meijer, U. Milkau, A. Moroni, W. F. J. Muller, C. Ngo, C. A. Ogilvie, J. Pochodzalla, G. Raciti, G. Rudolph, H. Sann, A. Schuttauf, W. Seidel, L. Stuttge, W. Trautmann, and A. Tucholski, Z. Phys. A **340**, 263 (1991).

[15] E. Plagnol, Nouv. Ganil **44**, 3 (1993).

[16] D. Drain *et al.*, Nucl. Instrum. Methods **A281**, 528 (1989).

[17] A. Lleres *et al.*, Phys. Rev. C (submitted).

[18] P. Désesquelles, Thèse, Université Joseph Fourier Grenoble I 1991.

[19] F. Benrachi *et al.*, Nucl. Instrum. Methods **A281**, 137 (1987).

[20] D. Drain *et al.*, in *First European Biennial Workshop on Nuclear Physics,* Megève, France, edited by D. Guinet and J. R. Pizzi (World Scientific, Singapore, 1991), p. 52.

[21] D. W. Stracener *et al.*, Nucl. Instrum. Methods A **294**, 485 (1990).

[22] A. J. Cole and P. Désesquelles, Z. Phys. A **337**, 71 (1990).

[23] M. Ploszajczak and A. Tucholski, Phys. Rev. Lett. **65**, 1539 (1990); Nucl. Phys. **A523**, 651 (1991).

[24] X. Campi, J. Phys. A **19**, L917 (1986); J. Phys. (Paris) **48**, C2-151 (1987); Phys. Lett. B **208**, 351 (1988).

[25] M. E. Brandan, A. J. Cole, P. Désesquelles, A. Giorni, D. Heuer, A. Lleres, A. Menchaca-Rocha, and K. Michaelian, Nucl. Phys. A (submitted).

[26] J. Péter *et al.*, Nucl. Phys. **A519**, 611 (1990).

[27] A. J. Cole, code BINFRAG (unpublished); see also K. Grotowski *et al.*, Phys. Lett. B **223**, 287 (1989).

[28] J. P. Bondorf, R. Donangelo, I. N. Mishustin, and H. Schulz, Nucl. Phys. **A444**, 460 (1985).

[29] X. C. Hu, Thèse, Université Claude Bernard, Lyon I, 1991.

[30] D. H. E. Gross, International Nuclear Physics Conference, Wiesbaden, Germany, 1992 (unpublished).

[31] U. Lynen *et al.*, Nucl. Phys. **A545**, 329c (1992); P. Kreutz *et al.*, Nucl. Phys. A (submitted).

[32] X. Campi, in *Chemical Physics of Atomic and Molecular Clusters,* Proceedings of the International School of Physics "E. Fermi," course 107, Varenna, Italy, edited by G. Scoles (Società Italiana di Fisica, Bologna, Italy, 1988).

[33] H. R. Jaqaman *et al.*, Nucl. Phys. **A514**, 327 (1990); H. R. Jaqaman and D. H. E. Gross, *ibid.* **A524**, 321 (1991).

[34] A. J. Cole, M. E. Brandan, P. Désesquelles, A. Giorni, D. Heuer, A. Lleres, A. Menchaca-Rocha, J. B. Viano, B. Chambon, B. Cheynis, D. Drain, and C. Pastor, Phys. Rev. C **47**, 1251 (1993).